AFRL-AFOSR-JP-TR-2022-0023

Refractory High Entropy Alloys for High Temperature Structural Applications

Budaraju, Srinivasa
INDIAN INSTITUTE OF TECHNOLOGY MADRAS
IITM,, ADYAR,
CHENNAI, TAMILNADU, 600036
IND

05/09/2022
Final Technical Report

Air Force Research Laboratory
Air Force Office of Scientific Research
Asian Office of Aerospace Research and Development
Unit 45002, APO AP 96338-5002

REPORT DOCUMENTATION PAGE

PLEASE DO NOT RETURN YOUR FORM TO THE ABOVE ORGANIZATION.

1. REPORT DATE	2. REPORT TYPE	3. DATES COVERED	
20220509	Final	START DATE 20180530	END DATE 20200529

4. TITLE AND SUBTITLE
Refractory High Entropy Alloys for High Temperature Structural Applications

5a. CONTRACT NUMBER	5b. GRANT NUMBER	5c. PROGRAM ELEMENT NUMBER
FA2386-18-1-4034		
5d. PROJECT NUMBER	**5e. TASK NUMBER**	**5f. WORK UNIT NUMBER**

6. AUTHOR(S)
Srinivasa Budaraju

7. PERFORMING ORGANIZATION NAME(S) AND ADDRESS(ES)
INDIAN INSTITUTE OF TECHNOLOGY MADRAS
IITM,, ADYAR,
CHENNAI, TAMILNADU 600036
IND

8. PERFORMING ORGANIZATION REPORT NUMBER

9. SPONSORING/MONITORING AGENCY NAME(S) AND ADDRESS(ES)	10. SPONSOR/MONITOR'S ACRONYM(S)	11. SPONSOR/MONITOR'S REPORT NUMBER(S)
AOARD UNIT 45002 APO AP 96338-5002	AFRL/AFOSR IOA	AFRL-AFOSR-JP-TR-2022-0023

12. DISTRIBUTION/AVAILABILITY STATEMENT
A Distribution Unlimited: PB Public Release

13. SUPPLEMENTARY NOTES

14. ABSTRACT
A methodology is developed for alloy selection based on rule-of-mixtures (ROM) combined with the CALculation of PHAse Diagram (CALPHAD) technique. All equiatomic quaternary and quinary equiatomic alloys based on Group-IV (Ti, Zr, Hf), Group-V (V, Nb, Ta), and Group-VI (Cr, Mo, W) are studied on density (Ï•), Young's modulus (E), specific heat at 1273K at constant pressure (Cp), liquidus temperature, valence electron concentration (VEC), and % atomic size difference/radius mismatch (Î´). Correlations between all the above six different parameters are studied using "scatter matrix" plot. The Scatter matrix plot approach gives a snapshot of all the properties of 126 quaternary and 126 quinary alloys. It helps in narrowing down the required alloy families based on design and application requirements.

15. SUBJECT TERMS

16. SECURITY CLASSIFICATION OF:			17. LIMITATION OF ABSTRACT	18. NUMBER OF PAGES
a. REPORT U	b. ABSTRACT U	c. THIS PAGE U	SAR	31

19a. NAME OF RESPONSIBLE PERSON	19b. PHONE NUMBER *(Include area code)*
JEREMY KNOPP	315-227-7006

REFRACTORY HIGH ENTROPY ALLOYS FOR HIGH TEMPERATURE STRUCTURAL APPLICATIONS

Prof. B.S. Murty

Department of Metallurgical and Materials Engineering

Indian Institute of Technology Madras

November/2020

Final Report

TABLE OF CONTENTS

Section **Page**

LIST OF FIGURES ii

LIST OF TABLES iii

1. SUMMARY 1

2. INTRODUCTION 1

3. METHODS, ASSUMPTIONS, AND PROCEDURES 3

3.1 Alloy design methodology 3

3.2 Synthesis of RHEA through powder metallurgy route 3

3.3 Powder metallurgy route (MA-air and MA-Ar) followed by SPS 5

3.4 Thermodynamic Calculations 5

4. RESULTS AND DISCUSSION 6

4.1 Density, liquidus temperature [10] 6

4.2 Young's Modulus [10] 6

4.3 Phases [10] 7

4.4 VEC Analysis [10] 7

4.5 Synthesis of CrMoNbTiW through MA+SPS 8

4.5.1 Phase evolution in dry milled MA_air_6h+SPS CrMoNbTiW 8

4.5.2 Phase evolution in dry milled MA_Ar_4h+SPS CrMoNbTiW 8

4.6 Validation of experimental results with CALPHAD 8

4.6.1. Calculated phase fraction plot for MA-air+SPS CrMoNbTiW 8

4.6.2. Comparison of MA-Ar-4h+SPS phase evolution with CALPHAD predictions 9

4.7 Microstructural stability after heat treatment (HT) at 1300 °C for 240 h 10

4.8 Summary of synthesis of RHEA through MA+SPS route 10

5. DEFORMATION AND STRENGTHENING MECHANISMS 10

5.1 Ductile-to-Brittle transition behavior 11

CONCLUSIONS 12

REFERENCES 13

LIST OF SYMBOLS, ABBREVIATIONS, AND ACRONYMS 26

LIST OF FIGURES

Page

Fig. 1 (a) Yield strength and (b) Specific Yield strength as a function of temperature. (c) Distribution of alloying elements in RHEAs. 17

Fig. 2 Scatter matrix plot of 4RHEAs. 18

Fig. 3 Scatter matrix plot of 5RHEAs. 19

Fig. 4 CALPHAD and ROM calculated density comparison for (a) 4RHEAs (b) 5RHEAs. 19

Fig. 5 Density correlated with VEC for (a) 4RHEAs (b) 5RHEAs. 20

Fig. 6 (a) Count of RHEAs with different number of phases. (b) Element counts in 1/2/3/4 phase 4RHEAs. (c) Count of RHEAs with different number of phases. (d) Element counts in 2/3/4/5 phase 5RHEAs. (e) Element counts in 4RHEAs of different VEC values 21

Fig. 7 XRD patterns of the MA powder (MA-air-6h and MA-Ar-4h) and sintered samples (MA-air-6h+SPS and MA-Ar-4h+SPS) showing the formation of secondary phases due to contamination from milling media and atmosphere 22

Fig. 8 (a) Lower magnification BSE-SEM micrograph of the MA-air-6h powder after sintering at 1300 °C and 50 MPa, (b) magnified image of the region inside the yellow box. (c) Phase map of the MA-air-6h+SPS CrMoNbTiW obtained via EBSD featuring the BCC, sigma, carbide, and oxide phases in red, green, yellow, and blue color, respectively, along with their grain size. 22

Fig. 9 (a) Lower magnification BSE-SEM micrograph of the MA-Ar-4h powder after sintering at 1500 °C and 50 MPa, (b) magnified image showing different phases. Blue, red, yellow, and pink dots represent grey (BCC1), white (BCC2), black (TiO1-xNx), and dark grey (Laves phase), respectively, and (c) Phase map of the MA-Ar-4h+SPS CrMoNbTiW obtained through EBSD featuring the BCC and TiO1-xNx phases in red and green color, respectively. 23

Fig. 10 Calculated phase fraction plot of (a) MA-air-6h+SPS and (b) MA-Ar-4h+SPS with C, and Fe and C, N, and Fe addition, respectively, to account for the formation of secondary phases, using TCHEA (v2.1). 23

Fig. 11 XRD pattern of CrMoNbTiW alloy synthesized through different routes after heat-treatment at 1300 °C for 240 h, illustrating the absence of any new phase formation. 24

Fig. 12 Slip planes in BCC with common slip direction [111]. 24

Fig. 13 (112) plane stacking sequence in BCC crystal. 24

Fig. 14 {110}<111> GSFE curve of Ta and Nb. 25

LIST OF TABLES

Page

Table 1 Formulae used for property estimation using ROM. 3
Table 2 ROM, CALPHAD, and experimental density comparison.....6

1 SUMMARY

In the present work, a methodology is developed for alloy selection based on rule-of-mixtures (ROM) combined with CALculation of PHAse Diagram (CALPHAD) technique. All equiatomic quaternary and quinary equiatomic alloys based on Group-IV (Ti, Zr, Hf), Group-V (V, Nb, Ta), and Group-VI (Cr, Mo, W) are studied on density (ρ), Young's modulus (E), specific heat at 1273K at constant pressure (C_p), liquidus temperature, valence electron concentration (VEC), and % atomic size difference/radius mismatch (δ). Correlations between all the above six different parameters are studied using "scatter matrix" plot. The Scatter matrix plot approach gives a snapshot of all the properties of 126 quaternary and 126 quinary alloys. It helps in narrowing down the required alloy families based on design and application requirements.

In the present study, MA+SPS is used to synthesis ultrafine-grained CrMoNbTiW RHEA. The MA parameters are varied to obtain an optimum extent of alloying with minimal contamination. The contaminants such as O, C, and N are measured after MA and SPS. MA in dry milling in ambient (air) and inert atmosphere (Argon) are termed as MA-AIR, and MA-Ar, respectively. MA-AIR+SPS resulted in the formation of a BCC solid solution, sigma, the Laves phase, and carbides, whereas 2BCC solid solutions, the Laves phase, and oxynitride phase was observed in MA-Ar+SPS. The formation of secondary phases is attributed to the presence of residual elements and contamination during MA. The phase formation at each step (MA, MA+SPS, cast) is compared with CALPHAD studies while accounting for the contamination. The usage of CALPHAD studies to predict the secondary phase formation in the non-equilibrium synthesis route gives an insight into the understanding of phase equilibria. Here, an attempt is made to understand the influence of synthesis routes on the phase formation of RHEA along with the CALPHAD studies and G-x curves.

The MA+SPS alloys are prone to grain growth due to its high surface area to volume ratio. Therefore, the thermal stability of these alloys is important. Also, there are no reports in the literature on the long-term thermal stability of RHEAs. Thus, the alloys in their as-synthesized state are subjected to a prolonged heat-treatment of 240 h at 1300 °C. The alloys' thermal stability in terms of the microstructure, grain size, and hardness are studied in detail. They exhibit exceptional coarsening resistance and show a negligible change in their grain size and hardness even after heat-treatment at 1300 °C for 240h.

2 INTRODUCTION

The demand for materials that can sustain higher temperatures for prolonged durations is increasing every day. Aerospace and power-generation industries have been at the forefront of developing alloys for extreme environments as they want to push the temperatures of their gas-turbines and jet-engines. The ever-increasing demand of higher part efficiencies and low specific-fuel consumptions has kept the materials scientists on their toes to develop new high-temperature materials. Conventional alloy design strategy relies heavily on improving the principal element's properties by adding alloying elements in minor quantities. The examples are: steels, which are based on Fe; superalloys, which are based on Ni, Co, or Fe; Intermetallics are based on compounds of Ni-Al, Ti-Al, Fe-Al, etc. In the last century, alloy development has reached its limits [1].

High entropy alloys (HEAs) is a new alloy design methodology in which there are more than one principal element. Since its proposal in 2004 by Yeh [1] and Cantor [2]. Unlike conventional alloys, where there's a principal element, HEAs does not have a single principal element. The concentration of each of the constituent element in HEA can vary between 5 to 35 at. % [1]. Equiatomic concentration maximizes the configurational entropy of the system, which may lead to suppression of intermetallics formation. The configurational entropy increases further the number of constituents in the alloy. The configurational entropy at

equiatomic concentrations of binary, ternary, quaternary, quinary, and sexinary alloys are 5.8, 9.2, 11.6, 13.5, and 15.0 J/mol/K, respectively. This is higher than the entropy fusion (7-11 J/mol/K) of most metals. The configurational space in the HEA design strategy is enormous compared to the conventional alloy design strategy, as large elemental concentrations are allowed [3,4].

Due to the freedom of multi-principal element, HEAs have shown excellent capabilities, such as high-temperature strength, toughness, ductility, wear-resistance, low neutron absorption, corrosion resistance [5]. Freedom from conventional restrictions on alloy composition have made HEAs the potential candidates for a variety of applications, including high-temperature applications *viz.*, aerospace, defense, and power-generation; lightweight materials, functional coatings, thermoelectric materials, high-frequency communication materials, hydrogen storage materials for mobile phones, *etc*.

The majority of HEA development work has been focused on transition metals, namely Fe, Co, Ni, and Cu. The high-temperature properties of HEAs can be improved with the use of refractory elements such as Ti, Zr, Hf (form Group-IV), V, Nb, Ta (from Group-V) and Cr, Mo, W (from Group-VI). The refractory HEAs (RHEAs) are being actively developed for high-temperature applications such as aerospace and power-generation industries. Starting from the seminal work of Senkov in 2010 [6], very little work has been done on the development of RHEAs having good combination of high-temperature strength and room temperature ductility.

The first RHEAs were developed as arc melted alloys containing Mo, Nb, Ta, V, and W. MoNbTaW and MoNbTaWV were the first RHEAs developed in the year 2010 [6]. These alloys have shown excellent strength retention capability even up to temperatures of about 1500 °C. This puts them in direct competition to currently used Ni-based superalloys. After these alloys, many more RHEAs were explored which contains Group IV (Ti, Zr, Hf), Group V (V, Nb, Ta) and Group VI (Cr, Mo, W) in the major proportion with minor additions of Al, Si, Co, and Ni. Minor additions have helped reduce the density of these alloys steadily. Fig. 1 shows the comparison between the various generation of superalloys, single-phase, and multiphase RHEAs in terms of their yield strength and specific yield strength [7]. Fig. 1 shows that most of the alloys lose their strength as the temperature increases beyond 1000 °C. Only MoNbTaWV (up to 1500 °C), MoNbTaW (up to 1500 °C), and CrTaVW (up to 1000 °C), have retained their strengths. It can also be observed that Al-containing alloys benefit from reduced density and improved specific strengths at the entire temperature range of study. This shows a direction to work on reducing the density of the RHEAs. Extensively studied RCCAs are HfNbTaTiZr [8], MoNbTaW [6], MoNbTaVW [6], NbTiVZr [9] and their non-equiatomic derivatives. Fig. 1(c) shows the distribution of alloying elements in reported RHEAs. It can be observed that most of the quinary and senary RCCAs contain Mo, Nb, Ti, V, and Zr. Due to their prohibitively high costs, Re and Os are not used in much of the alloys.

Based on the above literature survey, it was observed that the RHEAs can be made ductile at room temperature while maintaining their high-temperature strength. By diligently choosing the constituents and thermomechanical treatment, we can selectively eliminate or form different phases in the alloys, keeping the application-specific properties in mind. The traditional approach of alloy development requires one to synthesize and test a large number of alloys. As discussed before, the high melting points of RHEAs makes their property determination challenging. The present work is intended to develop a novel RHEA using the CALculation of PHase Diagram (CALPHAD) approach. It screens a large number of alloys and helps is narrowing down the alloy family based on design and application requirements. The deformation behavior of alloys is also studied, and an attempt is made to improve the room temperature ductility of alloys by studying their stacking fault energies.

3 METHODS, ASSUMPTIONS, AND PROCEDURES

3.1 Alloy Design Methodology

The majority of studied RHEAs are either quaternary or quinary alloys. Therefore, a total of 126 quaternary and 126 quinary alloys are studied on their density (ρ), Young's modulus (E), valence electron concentration (VEC), liquidus temperature, % atomic size difference (δ), and specific heat at constant pressure at 1273 K (C_p). The equiatomic alloys are selected from Ti, Zr, Hf (Group-IV), V, Nb, Ta (Group-V), and Cr, Mo, W (Group-VI) elements. They are designated as either quaternary RHEAs (4RHEA) or quinary RHEAs (5RHEA). Alloy properties are calculated using rule-of-mixtures (ROM) relations given in Table 1 [11,12]. The reference values of elements are taken from Ref. [13,14]. For CALPHAD calculations, Thermo-Calc software having TCHEA (v2.1) database is used to estimate alloy density (ρ), number of phases (at 298 K), and liquidus temperatures [15].

Table 1: Formulae used for property estimation using ROM.

Property	Formula
Density (g/cc)	$\rho_{alloy} = \frac{\sum_i (C \cdot A)_i}{\sum_i \left(\frac{C \cdot A}{\rho}\right)_i}$
Young's Modulus (GPa)	$E_{alloy} = \frac{\sum_i (C \cdot V \cdot E)_i}{\sum_i (C \cdot V)_i}$
%Radius mismatch/atomic size difference	$\delta = \sqrt{\sum_i C_i \cdot \left(1 - \frac{r_i}{\bar{r}}\right)^2}$
Valence Electron Concentration	$VEC = \sum_i C_i \cdot Valency_i$
Melting Point/Liquidus (K)	$T_m = \sum_i C_i \cdot T_i$
Specific heat at 1273 K (J/mol/K)	$C_p = \sum_i \left(C_p \cdot T\right)_i$

To get the overview of various properties and their inter-relations, the "scatter matrix" plot is given in Fig. 2 and Fig. 3 for 4RHEAs and 5RHEAs, respectively. In these two figures, 252 alloys have been studied on six different parameters [10]. The scatter matrix approach captures all the possible permutations between different properties with their correlation parameters (blue numbers in Fig. 2 and 3).

3.2 Synthesis of RHEA through powder metallurgy route

The RHEAs show considerable potential as ultra-high temperature materials due to their very high melting point (>2000 °C) and unique property of strength retention at elevated temperature [24,25]. The majority of RHEAs were synthesized using vacuum arc melting (VAM) besides a few studies by the mechanical alloying (MA) + spark plasma sintering (SPS) route.

The MA is a unique method to synthesize alloys from the elements having a high melting point and vast difference in vapor pressure [26],[27]. Through MA, grain refinement, improved

homogenization, and alloying can be achieved due to diffusion in a nanocrystalline state caused by repeated cold welding and fracturing of powder particles. Further, the consolidation of MA powders using SPS enables in retaining the nanostructures due to the shorter sintering duration; and dense pellets can be obtained owing to the simultaneous application of pressure and temperature. Although MA+SPS and VAM are widely used to synthesis various high entropy alloys (HEAs), studies on the effect of synthesis route on phase formation and microstructural evolution are very scarce. In each method, various process parameters are known to affect the microstructure. Accordingly, different microstructures have been reported for HEAs depending on the synthesis route [28–30]. In MA, the reactive metals (Al, Cr, Ti, V) can readily react with O, N, C (impurities from milling media/atmosphere/process control agent (PCA)) and form secondary phases. Therefore, the MA of reactive metals and alloys have to be dealt with caution [31–33].

From the literature, it is evident that there are only a handful of reports on the synthesis of the same RHEA composition through different processing routes[6,34–36]. Moreover, microstructural stability at high homologous temperatures (*e.g.*, >1200 °C) is a necessity for any high-temperature material. However, there are hardly any reports on the thermal stability of the RHEAs [37–39]. In general, the alloys synthesized through MA+SPS comprises secondary phases due to unsolicited contamination. Although these secondary phases (intermetallics, carbides, and/or oxides) increase the hardness, yield strength, and coarsening resistance [34,38,40–44], such unsolicited oxides and carbides reduce ductility and are thus undesirable [45]. Besides, any property enhancement resulting from secondary phases due to contamination is unintended and mostly uncontrollable.

In this context, it is worth acknowledging the research gaps that have not been addressed comprehensively in the RHEA literature. (a) The phase evolution during the MA of RHEA has not been explained in detail from the thermodynamics viewpoint, and its comparison with experimental observations and (b) the secondary phase formation due to contamination through the powder metallurgy route has not been accounted for while comparing with theoretical estimates such as CALPHAD studies. Although CALPHAD may not predict the phase equilibria accurately for non-equilibrium routes such as MA [46], specific thermodynamic trends and insights may be obtained to better understand phase equilibria. Raghavan *et al.* have compared the first phase to nucleate from liquid with that of MA, showing considerable agreement between experimental observations and predictions [47].

Therefore, exploring more RHEA systems becomes necessary. Accordingly, a novel RHEA system, Cr-Mo-Nb-Ti-W, is explored in the present study. The rationale behind choosing such an alloy comprising of these elements is the following. The elements such as Mo, Nb, W aid in retaining the strength at high-temperatures, and Cr and Ti helps in stabilizing the nanocrystalline nature of W-base alloys even after sintering. Thus CrMoNbTiW RHEA is synthesized to study the following: (i) to critically analyze the phase and microstructural evolution of CrMoNbTiW RHEA during two different processing routes of powder metallurgy (MA via dry milling (in air and Argon) + SPS) and casting route (VAM) to assess the role of processing route, (ii) to understand the microstructural stability of CrMoNbTiW (that was processed via two processing routes) at high temperatures for a longer duration, and (iii) to make a critical comparison of the microstructure and phase evolution during each processing step, *i.e.*, in the as-processed conditions (MA, MA+SPS, and as-cast) as well as after heat-treatment while correlating with CALPHAD studies. For effective and rationalistic use of CALPHAD studies in predicting and understanding the phase evolution through the MA+SPS route, the probable contaminants (C, O, and N) are also included in the CALPHAD analysis.

3.3 Powder metallurgy route (MA-air and MA-Ar) followed by SPS

For mechanical alloying in the air (MA-air), the elemental powders of Cr, Mo, Nb, Ti, and W (>99.5% purity) were used in equiatomic proportion. The MA was carried out in a horizontal high energy attritor mill (Simoloyer CM01-2l, Zoz GmbH, Germany) using stainless steel (SS) container, hard chrome steel balls of 5 mm diameter as the milling media (with 10:1 ball to powder weight ratio), and stearic acid (1 wt%.) as a process control agent (PCA). For mechanical alloying in Argon (MA-Ar), the milling container was initially evacuated to a vacuum of 10-1 mBar, followed by Ar purging (Ar purity of 99.995%). Around 20 mBar Ar pressure was maintained throughout the milling process. The milling chamber was cooled continuously by chilled water circulating through jacketed pipes. The powder samples were collected at regular intervals to analyze the phase evolution during MA using a PANalytical X'pert Pro X-ray diffraction (XRD) unit with Cu-Kα radiation. The MA powders were subsequently consolidated using spark plasma sintering (Dr. Sinter SPS-650, Sumitomo Coal Mining Co., Ltd, Japan) under vacuum (~10 Pa) at a heating rate of 100 °C min^{-1}. The MA-air powders were sintered at an optimized sintering temperature and pressure of 1300 °C and 50 MPa, respectively, with a holding duration of 2 min. For MA-Ar powders, sintering was done at different temperatures (1300 – 1500 °C) to get fully dense pellets.

The microstructural characterization of the alloys was carried out using FEI Quanta 400 FEG scanning electron microscope (SEM) operating at 20 kV equipped with an energy dispersive spectroscopy (EDS) attachment (for elemental composition analysis). During MA, contamination comes from the milling media – SS container with hard chrome steel balls (Fe), PCA – stearic acid (C), and atmosphere – air and Ar (O, N). Therefore, the contaminants such as carbon, nitrogen, and oxygen content of the MA powder were quantified using a LECO CS477 and LECO ONH836 analyzer, respectively, whereas the Fe contamination was quantified through SEM-EDS analysis. Detailed phase and microstructural analysis were performed with a step size of 50 nm using Helios G4 UX (FE-SEM) equipped with electron backscatter diffraction (HIKARI PRO EBSD) attachment. The volume fraction of the phases was calculated from the BSE-SEM image analysis using ImageJ software. The reported phase fractions are an outcome of the analysis of 10 BSE-SEM images. The EBSD results were analyzed using TSL-OIM software to obtain the grain size of different phases. Hardness measurements were carried out on the cross-section of the SPS-consolidated and cast samples using a Wolpert Wilson Vickers hardness instrument at a load of 500 g with a dwell time of 10 seconds. The reported hardness values are an average of at least ten measurements.

3.4 Thermodynamic Calculations

All the calculations for CALPHAD studies were executed using Thermo-Calc software [48,49] in combination with TCHEA (v2.1) database. Independent equilibrium phase fraction plots (phase fraction vs. temperature) were calculated for the powder metallurgy and casting routes. For the powder metallurgy route, an experimentally measured quantity of iron, carbon, and nitrogen from the sintered samples were added to the calculations to account for the contamination. The details of the contamination in the MA powders are discussed in Section 4.5.1 and 4.5.2. The O contamination was also observed in the MA powders. However, O contamination was not included in the calculations since TCHEA (v2.1) does not have Gibbs energy (G) data for phases with O. The overall composition of the sintered sample was considered while accounting for Fe, C, and N in the calculation. Additionally, binary G–x plots (x is composition) [50] were also calculated in certain cases to gain a better understanding of the phase formation. The BCC was used as the reference state in the G-x plots for ease of analysis.

4 RESULTS AND DISCUSSION

4.1 Density, liquidus temperature [10]

Density calculated using ROM and CALPHAD approach are compared in Fig. 4(a) and (b). TiZrVCr (6.03 g/cm^3) and TiZrVCrNb (6.57 g/cm^3) have the lowest density; whereas, the heaviest are MoTaWHf (14.81 g/cm^3) and MoTaWHfCr (13.72 g/cm^3). ROM, CALPHAD, and experimental densities of a few RHEAs are compared in Table 2. The values are closely matching with experimental densities.

Liquidus temperature calculated using ROM (MP-ROM) and CALPHAD (MP-TC) approach are compared in Fig. 4(c) and (d). TiZrVCr (MP-ROM=2108 K, MP-TC=1623 K) and TiZrVCrHf (MP-ROM=2187 K, MP-TC=1621 K) have the lowest liquidus temperature; whereas, MoNbTaW (MP-ROM=3158 K, MP-TC=3138 K) and MoNbTaWV (MP-ROM=2963 K, MP-TC=2976 K) have the highest liquidus temperature. For both the alloy families, density is well-correlated with MP-TC, as shown by the correlation parameter of 0.69 in Fig. 2 and 3 (number in blue color). Four distinct groups are observed when density is plotted against MP-TC in Fig. 4. In each of these groups, density is increasing with VEC, as shown by the positive slope of the trend line. In Fig. 5, as we go from trend line (1) to (4), the amount of Group-VI (Cr, Mo, W) decreases, and the amount of Group-IV (Ti, Zr, Hf) increases.

There is no report on experimentally determined liquidus temperature of RHEAs. Therefore, CALPHAD technique can be used to gives an estimate of the liquidus temperature of RHEAs. There is a deviation of ROM calculated liquidus temperature values from CALPHAD estimated values, as observed in Fig. 4(c) and (d). This is due to the thermodynamic basis of the CALPHAD approach, which considers the interaction between the elements, whereas ROM does not take that into account.

Table 2: ROM, CALPHAD, and experimental density comparison.

S. No.	Alloy	Experimental ρ (g/cm^3)	ROM ρ (g/cm^3)	CALPHAD ρ (g/cm^3)	Reference (for experimental ρ)
			Present work		
1	MoNbTaW	13.64	13.75	13.8	[6]
2	MoNbTaWV	12.36	12.36	12.44	
3	NbTiVZr	6.52	6.5	6.4	[12]
4	CrNbTiZr	6.67	6.7	6.73	
5	CrNbTiVZr	6.57	6.52	6.68	
6	TiZrHfNbTa	9.94	9.91	9.89	[13]
7	TiZrHfMoTa	10.24	10.21	10.19	[14]
8	MoNbTaTiW	11.72	11.76	11.85	[9]
9	NbTiZrVMo	7.27	7.13	7.18	
10	NbTiZrVTa	8.43	8.5	8.5	
11	NbTiZrVCr	6.57	6.57	6.68	

4.2 Young's Modulus [10]

In both 4RHEAs and 5RHEAs, the E is directly affected by MP-TC, ρ, and VEC, as observed from Figs. 2, 3 and 4. For 4RHEAs, TiZrHfNb has the lowest E of 89.37 GPa, and TaCrMoW has the highest E of 298.23 GPa. For 5RHEAs, TiZrHfNbV has the lowest E of 94.99 GPa, and TaCrMoWV has the highest E of 266.93 GPa. For 4RHEAs, E is strongly correlated with MP-TC, ρ, and VEC, as shown by the respective correlation parameter of 0.75, 0.52, and 0.90 (Fig. 2). For 5RHEAs, E is strongly correlated with MP-TC, ρ, and VEC, as shown by the respective correlation parameter of 0.76, 0.51, and 0.90 (Fig. 3). From the ductility criteria of VEC = 4.5 [11], TiZrHfTa, TiZrVTa, TiZrHfV, TiZrHfTaNb, TiZrHfVTa,

and TiZrHfVNb alloys can possess good ductility among the studied 4RHEAs and 5RHEAs, whereas, CrMoWTa, CrMoWNb, CrMoWNbTa, CrMoWVT, a, and CrMoWVNb alloys can possess poor ductility among the studied alloys (Fig. 5). For both 4RHEAs and 5RHEAs, from Figs. 5(a) and (b), the majority of alloys near trendline (1) has Ti, Zr, and Hf in them; in contrast, the majority of alloys near trendline (4) has Cr, Mo, and W in them.

4.3 Phases [10]

From Fig. 6(a) and (c), among all the 252 studied 4RHEAs and 5RHEAs, there is only one single-phase alloy (MoNbTaW) and only one five-phase alloy (TiVTaCrMo). Forty 4RHEAs and 18 5RHEAs have a two-phase microstructure. Seventy-one 4RHEAs and 84 5RHEAs have a three-phase microstructure. Fourteen 4RHEAs and 23 5RHEAs have a four-phase microstructure. The majority of the studied alloys have a three-phase microstructure (155 alloys). These three-phase alloys have a high occurrence of Ti, Zr, and Hf in them (Fig. 6(b) and (d)).

Increased entropy does not help the RHEAs become a single phase, as observed in Figure 6 (a) and (c). It suggests that along with entropy of mixing, the enthalpy of mixing should also be considered while deciding the phase formation rules [12,15]. From Fig. 6(b), Zr, Hf, and Nb are helping the 4RHEAs to have three-phase microstructure; and Ti, Ta are helping them to have four-phase microstructure. Similarly, from Fig. 6(d), Ti, Zr, and Hf are helping the 5RHEAs to have a three-phase microstructure.

4.4 VEC Analysis [10]

From Fig. 6(e) and (f) and from the ductility criteria of VEC < 4.5 [11], among them, studied 252 RHEAs, Ti, Zr, and Hf containing alloys can show good ductility, whereas Cr, Mo, and W containing alloys can show poor ductility. From Fig. 6(a) and (b), TiZrHfV, TiZrHfNb, TiZrHfTa (4RHEAs, VEC=4.25) and TiZrHfVNb, TiZrHfVTa, TiZrHfNbTa (5RHEAs, VEC=4.4) can show high ductility. Similarly, TaCrMoW, NbCrMoW, VCrMoW (4RHEAs, VEC=5.75) and NbTaCrMoW, VTaCrMoW, VNbCrMoW (5RHEAs, VEC=5.6). Young's modulus (E) comparison with density for (a) 4RHEAs (b) 5RHEAs can show poor ductility. These observations are similar to earlier works on TiZrHfNbTa and TiZrHfMoTa alloys [13,14,16–18].

The increase in ρ and E is directly influenced by the increase in VEC. It can be explained by the reduction in the molar volume of the over alloy. The trend of decreasing molar volume with increased valency of elements is common in the periodic table [19]. As we traverse from Group-IV (Ti, Zr, Hf) to Group-VI (Cr, Mo, W), the valency and protons in the atom increases. The increased positive charge on the nucleus attracts the electron cloud towards it and reduces the atomic size. Reduction in atomic size reduces the molar volume of the element. Decreased molar volume with high atomic weight increases the overall density of the alloys. Therefore, a higher fraction of Group-VI elements than Group-IV elements results in increased VEC and decreased average atomic size of the alloy, which decreases the overall molar volume of the alloy. Similarly, higher amounts of Group-VI elements lead to a higher average atomic weight of the alloy. Therefore, the alloy density increases. With the same approach, the VEC increase leads to the strengthening of bonds between alloy atoms, which leads to higher liquidus temperatures and improved E.

In ductile alloys, the dislocations are nucleated before cracks. Whenever the local shear stresses on the slip plane go beyond the alloy's ideal shear strength, dislocation nucleates. In contrast, crack initiation happens when the tensile stresses greater than the alloy's tensile strength acts in the direction perpendicular to the cleavage plane [20]. Some alloys have failed in shear deformation mode with no cracking, even when they were loaded in tensile mode

perpendicular to their cleavage plane [21]. This is known as “shear instability”, when dislocations get triggered before the cracks, and alloy becomes “intrinsically ductile”. If the shear instability appears after the tensile strength, then the alloy is called to be “intrinsically brittle”. Mo and W are examples of “intrinsically brittle” metals. They have been made into ductile alloys by appropriate alloying additions, which reduces their VEC and induces Jahn-Teller distortion [22]. A similar approach is used to ductilize RHEAs by reducing their overall VEC with alloying [11,23]. Intrinsic ductility can be induced in RHEAs by alloying with low valency elements. In the current study, Ti, Zr, and Hf can help in ductilizing the RHEAs, as these Group-IV elements have the lowest valency among the studied Group-IV (Ti, Zr, Hf), Group-V (V, Nb, Ta) and Group-VI (Cr, Mo, W) elements (Fig. 6(e) and (f)). Similarly, Cr, Mo, and W can help in making the RHEAs brittle (Fig. 6(e) and (f)).

4.5 Synthesis of CrMoNbTiW through MA+SPS

4.5.1. Phase evolution in dry milled MA_air_6h+SPS CrMoNbTiW

The MA_6h showed single-phase BCC along with undissolved Cr and Nb (Fig. 7). SPS was done at the optimized condition of 1300 °C with 50 MPa for a holding time of 2 min.

The alloy after sintering at 1300°C had 99 % relative density with respect to the theoretical density of 9.95 g/cm^3. The phase formation of the sintered sample was analyzed using XRD studies. The sintered sample showed the presence of a mixed carbide {(NbTi)C}, sigma phase {FeCr}, oxide {TiO_2}, and BCC phase, as presented in Fig. 7. The phases observed from XRD studies were confirmed with SEM analysis (Fig. 8). The formation of sigma phase is attributed to the Fe contamination from the milling media. Ti being a strong oxide former, forms TiO_2; further, Nb and Ti combine to form the mixed (NbTi)C. Thus, the undissolved Cr combines with the Fe contamination and forms sigma phase. In this case, Laves phase is not formed due to the unavailability of free Nb, as Nb has already formed a mixed carbide. The grain size of the phases was identified using EBSD analysis with a step size of 50 nm.

4.5.2. Phase evolution in dry milled MA_Ar_4h+SPS CrMoNbTiW

The CrMoNbTiW was synthesized through MA in an argon atmosphere to minimize the contamination, which was observed when the same alloy was milled in an air atmosphere. The alloy was milled for 4h in Ar atmosphere, and SPS was done at different temperatures (1300, 1400, and 1500 ºC) to get the optimum density. The XRD pattern of the 4h MA and sintered pellet is as shown in Fig. 7. After 4h of MA, a BCC solid solution along with residual Cr and Nb were observed. The MA powder was sintered at 1500 ºC to get a completely dense pellet. The sintered samples consisted of two BCC solid solutions along with Cr_2Nb Laves phase and $TiO_{1-x}N_x$ as shown in Fig. 9. The light grey, bright, dark grey, and black regions correspond to BCC 1, BCC 2, Laves, and $TiO_{1-x}N_x$ phase, respectively. The XRD pattern of the 1500 ºC sintered sample shows the presence of BCC solid solution and $TiO_{1-x}N_x$. The SEM-EDS analysis confirms the presence of second BCC phase and Cr_2Nb Laves phase. The volume fraction of BCC 1, BCC 2, Cr_2Nb Laves, and $TiO_{1-x}N_x$ was 84.4, 0.3, 3.6, and 11.7 %, respectively, from SEM image analysis. For the EBSD analysis (Fig. 9), generic BCC and TiN (same crystal structure ($Fm\bar{3}m$) [51]) and the closer lattice parameter (0.418 nm, ICSD PDF #23-6801 as that of $TiO_{1-x}N_x$) were used as the standard files.

4.6 Validation of experimental results with CALPHAD

4.6.1. Calculated phase fraction plot for MA-air+SPS CrMoNbTiW

The phase fraction plot obtained via CALPHAD studies while accounting for contamination MA-air-6h+SPS (C and Fe of 7.5 and 5.0 at.%, respectively) is shown in Fig. 10(a). The phases that are calculated to be in equilibrium at 1300 °C (sintering temperature) are BCC1, Cr_2Ti (C14), and TiC. The CALPHAD studies did not predict the formation of

secondary phases, such as σ and mixed carbides accurately. Moreover, CALPHAD predicted three BCC phases in contrast to just one BCC phase. Among the alloying elements used in the study, Ti has the strongest affinity towards oxygen, leading to the formation of Ti-rich oxide [52]. Since O is not included in the TCHEA (v2.1) database, this phase could not be calculated. Therefore, there is a large discrepancy in Ti content in the calculated and observed BCC phase. (ii) CALPHAD studies show TiC to be stable, but experimentally a carbide rich in Nb and Ti was seen. This disagreement is due to the consequence of Ti-oxide formation, as it replenished the availability of Ti for carbide formation.

The Gibbs energy of TiC and NbC were calculated to be –317.86 and –307.49 kJ mol^{-1}, respectively. (iii) The Laves phase (Cr_2Ti), which is estimated to be stable through CALPHAD, did not form experimentally. This inconsistency is possibly due to the unavailability of Ti after oxide and carbide formation. The experimental observation of σ-phase also did not match with the calculations. The observed composition and crystal structure of σ are close to that of FeCr-sigma (JCPDS No. 005-0708). Therefore, most of the residual Cr (after MA) appears to have combined with Fe contaminant and resulted in the formation of σ (after SPS).

4.6.2. Comparison of MA-Ar-4h+SPS phase evolution with CALPHAD predictions

The phase fraction plot of MA-Ar-4h+SPS while accounting for the contamination (carbon, nitrogen, and iron of 0.77, 1.02, and 2.46 at.%, respectively) is shown in Fig. 10(b). The equilibrium phases at 1500 °C (sintering temperature) are BCC1 and TiC. Two BCC solid solution along with $(Cr,Fe)_2(Nb,Ti)$ Laves phase and TiO1-xNx were observed experimentally. The formation of the Laves phase and TiO1-xNx is not reflected in the CALPHAD prediction.

Among the alloying elements used in the study, Ti has the strongest affinity towards oxygen and nitrogen, leading to the formation of the Ti-rich oxide nitride phase [52,53]. Since O is not included in the TCHEA (v2.1) database, this phase could not be calculated. Therefore, there is a large discrepancy in Ti content in the calculated and observed BCC phase. (ii) CALPHAD studies show TiC to be stable, but experimentally it is not observed. This disagreement is possibly due to the consequence of $TiO_{1-x}N_x$ formation, as it exhausted the reservoir of Ti for carbide formation. Moreover, the amount of C contamination is reduced (by about an order) by eliminating PCA toluene while carrying out MA in Ar atmosphere, leading to kinetic constraints in the formation of TiC. (iii) The Laves phase, which is experimentally observed, is not reflected in the prediction. From Fig. 10, it can be seen that the Laves phase (Cr_2Ti with C14 and C15 crystal structure) is not stable above 1350 ºC. The presence of residual Cr and Nb in MA-Ar-4h powder resulted in the formation of the Laves phase with some dissolved Fe (contamination) after SPS.

Ti has the strongest affinity towards O and N. Moreover, among oxygen and nitrogen, the affinity of Ti towards oxygen is much higher than nitrogen [52,54,55]. Further, in the MA-air-6h+SPS route, although the availability of N is abundant in the ambient atmosphere, the Ti-O reaction dominates due to the slow diffusion of N in Ti [55,56]. Unlike the MA-air-6h+SPS route, the availability of O is limited, and oxygen pick up is lower for the MA-Ar-4h+SPS route. Therefore, in such a scenario, the reaction of Ti-O becomes unfavorable, leading to the formation of a non-stoichiometric Ti-O-N compound. The probability of the formation of such non-stoichiometric compounds can be better understood by looking into their binary or ternary phase diagram. Due to the unavailability of the ternary Ti-O-N phase diagram, the binary phase diagrams of Ti-O [57] and Ti-N [51] can be considered for the $TiO_{1-x}N_x$ phase formation. It can be inferred from the binary phase diagrams that both TiO and TiN are isostructural $Fm\bar{3}m$ compounds with a wide solubility range, indicating that they possibly extend to the ternary composition space.

4.7 Microstructural stability after heat treatment (HT) at 1300 °C for 240 h

The XRD patterns of the alloy at different routes (MA-air-6h+SPS, MA-Ar-4h+SPS, and cast) after HT at 1300 °C for 240 h are shown in Fig. 11. It is interesting to note that the phases found in the as-synthesized conditions are present without the formation of any new phase after a long duration of heat treatment 1300 °C. The composition and volume fraction of the phases were observed to approach equilibrium values. The heat treatment duration was decided based on the diffusion coefficient of the alloying elements and grain size of the BCC phase, according to the equation, $x = \sqrt{Dt}$. The grain size of the BCC phase was found to be 270 ± 5 nm. Assuming a diffusion distance of thrice the grain size (~ 1 μm), the time was calculated based on the diffusion coefficient of the slowest diffusing species at 1300 ºC. Among the alloying elements, Nb was found to be the slowest diffusing species. Thus, the alloy was heat-treated at 1300 ºC for 10 days. It was found that the amount of BCC phase decreases with heat treatment, whereas the reverse is observed for the intermetallic phases like Laves and sigma phase. The Cr diffuses from the BCC phase and goes into the Laves phase or sigma phase. Thus, the BCC phase acts as a reservoir of Cr, Nb, and Ti to form Laves phase, sigma phase, and Ti rich carbides and oxides.

4.8 Summary of synthesis of RHEA through MA+SPS route

The following are the important points based on critical analysis of the experimental observations together with a comparison with CALPHAD studies.

1. The milling atmosphere (air and Ar) plays a significant role in the microstructural and phase evolution during the MA of reactive alloys such as the present RHEA. The incomplete alloying during MA and contamination from the milling media lead to the formation of secondary phases. The extent of the formation of these secondary phases depends on the MA parameters.
2. After SPS, the MA-air-6h+SPS route resulted in the formation of BCC, σ, (Nb, Ti)C and TiO_2, whereas two BCC solid solution phases along with the Laves phase and $TiO_{1-x}N_x$ were observed in the MA-Ar-4h+SPS path. The presence of various secondary phases such as σ, carbides, and oxides along with fine grain size resulted in a higher hardness of the sintered sample as compared to the cast alloy and MA-Ar-4h+SPS alloy.
3. In the CALPHAD study of CrMoNbTiW with Fe and C addition (MA+SPS), discrepancies were observed in the phase formation due to the limitation of the TCHEA (v2.1) database besides the characteristics of the processing routes. However, the CALPHAD studies are relatively consistent with the prediction of the BCC phase in the MA+SPS route.
4. The present investigation is the first report in the RHEA literature to show excellent thermal stability of the microstructure with no new phase formation during heat-treatment (HT) at 1300 °C for a prolonged duration of 240 h. It is apparent from this work that, for metastable processing routes such as MA, kinetics associated with the processing route has the upper hand over thermodynamics in case of phase formation.
5. The present comprehensive study on the processing of CrMoNbTiW RHEA by various routes clearly illustrates the persistent issues with MA (in air and Ar) such as inevitable contamination resulting in inadequate alloying, leading to the formation of undesirable phases. Therefore, a more efficient method of processing RHEAs is a bigger challenge in the research area of ultra-high temperature materials. One such effective way that can be considered is the use of pre-alloyed gas atomized powders for consolidation.

5 DEFORMATION AND STRENGTHENING MECHANISMS

Most of the RHEAs are BCC in nature; hence evaluating the underlying deformation mechanisms has remained a challenge. BCC crystal structure clubbed with different elements in large proportions create a challenge in defining the exact slip planes. The three slip planes

$\{110\}, \{112\}, \text{and} \{23\}$ with common <111> slip direction in BCC metals/alloys does not become active at the same time. Some of them get activated at higher temperatures. Hence finding out the exact slip plane and direction becomes difficult [58]. All three slip planes have at least one common close-packed <111> direction; due to this, the dislocation can cross slip from one plane to another.

HfNbTaTiZr is the first alloy among RHEAs, which has shown the highest room temperature (RT) compressive ductility of about 50% [8]. This was an attempt to improve RT ductility as well as to reduce the density of RCCAs. The MoNbTaVW alloy (first RCCA) was taken into consideration, which has a density of about 13.75 g/cc and a melting point of about 2689 °C. By replacing heavy Mo, V, and W with Hf, Ti, and Zr, the alloy density was reduced to 9.94 g/cc, and the melting point was calculated to be 2250 °C. This alloy has shown deformation banding and twinning, which has led to strain hardening. As previously stated, the alloy has single phase BCC structure before and after cold rolling. This gets transformed into two different BCC phases after annealing between 800 and 1000 °C. Hence, the single-phase BCC should be considered as a meta-stable phase. This observation and low diffusivities of individual refractory elements make the equilibrium phase stabilization difficult in RCCAs. Even after prolonged heat treatment of 24 h at 1200 °C followed by furnace cooling, it could not prevent the transformation of single-phase BCC into two separate equilibrium BCC phases (one rich in Hf and Zr, other rich in Nb and Ta).

Strengthening mechanisms in RCCAs is directly linked with their underlying deformation mechanisms. If the deformation occurs by dislocation slip, then any obstruction to dislocation motion can be considered a strengthening mechanism. Similarly, Hall-Petch strengthening can also be employed by reducing grain size (Hall 1951; Petch. 1953). RHEAs have constituent elements in large quantities; there is no concept of solute and solvent; this leads to a large variation in modulus in the path of a moving dislocation. Hence, it is observed that these alloys are inherently strong. But the problem comes when they start losing their ductility in RT ranges. Strengthening mechanisms observed/proposed so far in RHEAs/RCCAs can be listed as below:

i) Hall-Petch strengthening
ii) Deformation twinning
iii) Severe lattice distortion
iv) Solid solution strengthening
v) Precipitation hardening

5.1 Ductile-to-Brittle transition behavior

Like any other BCC metals and alloys, RHEAs also suffer from ductile-to-brittle transformation temperature (DBTT) issue. Above a certain temperature, the alloys behave in a ductile manner in which the alloy can accommodate relatively large strains. Below a certain temperature, the alloys become brittle with strain accommodation <1%. This temperature is called DBTT or brittle-to-ductile transition temperature (BDT).

$$\text{brittle behavior} < T_{BDT} < \text{ductile behavior}$$

To ductilize RHEAs over wide temperature ranges, it has been observed that additions of group IV elements (Ti, Zr, and Hf) help it. First principle calculations have concluded that brittle metals like Mo and W can be made ductile by adding group IV and V metals. This has been explained by modification in the metals' electronic structure, which leads to Jahn–Teller distortion. The alloy can be made ductile at RT by reducing its DBTT to temperatures below RT. This can be done if the alloy is made to accommodate large strains by making it susceptible to twinning by tuning its stacking fault energy (SFE). As the energy of fault increases, the fault width decreases since the interaction between the dislocation partials reduces. Reduced SFE makes the metal alloy susceptible to twinning, which gives a right combination of strength and ductility [59]. The entire phenomenon can be explained as below,

Low SFE → Large SF width → Less interaction between dislocation partials → Dislocations cannot combine easily → Difficult cross-slip → Easy twinning → Large strain accumulation

In BCC systems we do not exactly know the close-packed plane on which slip occurs (Fig. 12). In BCC if we consider the {112} planes, then the stacking sequence becomes (Fig. 13) [60,61],

…ABCDEFABCDEFABCDEF…

One complete stacking sequence consists of 6 planes of {112} type [62]. The exact change in stacking sequence depends on what all planes are getting faulted (Fig. 13). In this wide stacking sequence, which plane will lead to the fault, is difficult to define.

The energy of this intrinsic SF can be defined as,

$$\gamma_{intrinsic} = \frac{E_{faulted} - E_{pristine}}{Area\ of\ fault}$$

Fig. 14 shows the GSFE curve of Nb and Ta for {110}<111> slip system. Nb and Ta both the metals belong to Group-IV of the periodic table with a same crystal structure. This gives a direction of reducing the SFE of an initially brittle metal by alloying it with an element of lower SFE. The reduced SFE can lead to the overall toughening of the alloy as [63].

6. CONCLUSIONS

ROM technique, in combination with CALPHAD, can act as a useful methodology to narrow down alloy system for detailed study. It can reduce the number of test samples to be synthesized and analyzed, ultimately leading to shorter development times.

Synthesis of RHEA through MA+SPS must be dealt with caution. More promising methods, such as the use of pre-alloyed powders, can be used to avoid any kind of contamination during the synthesis stage. The high-temperature strength retention of most of the RHEAs is attributed to the solid solution strengthening. In HEAs, the lattice distortion due to the presence of different elements leads to solid solution strengthening. In alloys containing Al, Zr, Hf, the strength is due to the presence of B2 phase along with Al-Zr intermetallic phase. Another important point to note is the thermal stability of these RHEAs. Most of the alloys undergo precipitation or phase separation during long term annealing or deformation.

REFERENCES

[1] J.W. Yeh, S.K. Chen, S.J. Lin, J.Y. Gan, T.S. Chin, T.T. Shun, C.H. Tsau, S.Y. Chang, Nanostructured high-entropy alloys with multiple principal elements: Novel alloy design concepts and outcomes, Adv. Eng. Mater. 6 (2004) 299-303+274. https://doi.org/10.1002/adem.200300567.

[2] B. Cantor, I.T.H. Chang, P. Knight, A.J.B. Vincent, Microstructural development in equiatomic multicomponent alloys, Mater. Sci. Eng. A. 375–377 (2004) 213–218. https://doi.org/10.1016/j.msea.2003.10.257.

[3] S. Gorsse, D.B. Miracle, O.N. Senkov, Mapping the world of complex concentrated alloys, Acta Mater. 135 (2017) 177–187. https://doi.org/10.1016/j.actamat.2017.06.027.

[4] B.S. Murty, J.W. Yeh, S. Ranganathan, P.P. Bhattacharjee, eds., Index, in: High-Entropy Alloy. (Second Ed., Second Edi, Elsevier, 2019: pp. 355–363. https://doi.org/https://doi.org/10.1016/B978-0-12-816067-1.09981-1.

[5] J.W. Yeh, Recent progress in high-entropy alloys, Ann. Chim. Sci. Des Mater. 31 (2006) 633–648. https://doi.org/10.3166/acsm.31.633-648.

[6] O.N. Senkov, G.B. Wilks, D.B. Miracle, C.P. Chuang, P.K. Liaw, Refractory high-entropy alloys, Intermetallics. 18 (2010) 1758–1765. https://doi.org/10.1016/j.intermet.2010.05.014.

[7] O.N. Senkov, D.B. Miracle, K.J. Chaput, J.-P. Couzinie, Development and exploration of refractory high entropy alloys—A review, J. Mater. Res. 33 (2018) 3092–3128. https://doi.org/10.1557/jmr.2018.153.

[8] O.N. Senkov, J.M. Scott, S.V. Senkova, D.B. Miracle, C.F. Woodward, Microstructure and room temperature properties of a high-entropy TaNbHfZrTi alloy, J. Alloys Compd. 509 (2011) 6043–6048. https://doi.org/10.1016/j.jallcom.2011.02.171.

[9] O.N. Senkov, S. Rao, K.J. Chaput, C. Woodward, Compositional effect on microstructure and properties of NbTiZr-based complex concentrated alloys, Acta Mater. 151 (2018) 201–215. https://doi.org/10.1016/j.actamat.2018.03.065.

[10] S.M. Shaikh, V.S. Hariharan, S.K. Yadav, B.S. Murty, CALPHAD and rule-of-mixtures: A comparative study for refractory high entropy alloys, Intermetallics. 127 (2020) 106926. https://doi.org/10.1016/j.intermet.2020.106926.

[11] S. Sheikh, S. Shafeie, Q. Hu, J. Ahlström, C. Persson, J. Veselý, J. Zýka, U. Klement, S. Guo, Alloy design for intrinsically ductile refractory high-entropy alloys, J. Appl. Phys. 120 (2016) 164902. https://doi.org/10.1063/1.4966659.

[12] O.N. Senkov, S. V. Senkova, C. Woodward, D.B. Miracle, Low-density, refractory multi-principal element alloys of the Cr-Nb-Ti-V-Zr system: Microstructure and phase analysis, Acta Mater. 61 (2013) 1545–1557. https://doi.org/10.1016/j.actamat.2012.11.032.

[13] O.N. Senkov, J.M. Scott, S. V. Senkova, F. Meisenkothen, D.B. Miracle, C.F. Woodward, Microstructure and elevated temperature properties of a refractory TaNbHfZrTi alloy, J. Mater. Sci. 47 (2012) 4062–4074. https://doi.org/10.1007/s10853-012-6260-2.

[14] C.C. Juan, M.H. Tsai, C.W. Tsai, C.M. Lin, W.R. Wang, C.C. Yang, S.K. Chen, S.J. Lin, J.W. Yeh, Enhanced mechanical properties of HfMoTaTiZr and HfMoNbTaTiZr refractory high-entropy alloys, Intermetallics. 62 (2015) 76–83. https://doi.org/10.1016/j.intermet.2015.03.013.

[15] O.N. Senkov, J.D. Miller, D.B. Miracle, C. Woodward, Accelerated exploration of multi-principal element alloys with solid solution phases, Nat. Commun. 6 (2015) 1–10. https://doi.org/10.1038/ncomms7529.

[16] O.N. Senkov, S.L. Semiatin, Microstructure and properties of a refractory high-entropy alloy after cold working, J. Alloys Compd. 649 (2015) 1110–1123.

https://doi.org/10.1016/j.jallcom.2015.07.209.
[17] L. Lilensten, J.P. Couzinié, L. Perrière, A. Hocini, C. Keller, G. Dirras, I. Guillot, Study of a bcc multi-principal element alloy: Tensile and simple shear properties and underlying deformation mechanisms, Acta Mater. (2018). https://doi.org/10.1016/j.actamat.2017.09.062.
[18] C.C. Juan, M.H. Tsai, C.W. Tsai, W.L. Hsu, C.M. Lin, S.K. Chen, S.J. Lin, J.W. Yeh, Simultaneously increasing the strength and ductility of a refractory high-entropy alloy via grain refining, Mater. Lett. 184 (2016) 200–203. https://doi.org/10.1016/j.matlet.2016.08.060.
[19] M. Dayah, Ptable: Periodic Table, Ptable. (1997). https://ptable.com (accessed November 3, 2020).
[20] A. Kelly, N.H. Macmillan, Strong solids, Clarendon Press, 1986. https://books.google.co.in/books?id=z5NRAAAAMAAJ.
[21] J.W. Morris, C.R. Krenn, The internal stability of an elastic solid, Philos. Mag. A. 80 (2000) 2827–2840. https://doi.org/10.1080/01418610008223897.
[22] H.A. JAHN, E. TELLER, Stability of Polyatomic Molecules in Degenerate Electronic States I. Orbital Degeneracy, Appl. Gr. Theory. (1968) 233–255. https://doi.org/10.1016/b978-0-08-203190-1.50014-7.
[23] T. Yang, Y.L. Zhao, W.H. Liu, J.H. Zhu, J.J. Kai, C.T. Liu, Ductilizing brittle high-entropy alloys via tailoring valence electron concentrations of precipitates by controlled elemental partitioning, Mater. Res. Lett. 6 (2018) 600–606. https://doi.org/10.1080/21663831.2018.1518276.
[24] O.N. Senkov, D.B. Miracle, K.J. Chaput, J.P. Couzinie, Development and exploration of refractory high entropy alloys - A review, J. Mater. Res. 33 (2018) 3092–3128. https://doi.org/10.1557/jmr.2018.153.
[25] S. Praveen, H.S. Kim, High-Entropy Alloys: Potential Candidates for High-Temperature Applications – An Overview, Adv. Eng. Mater. 20 (2018) 1–22. https://doi.org/10.1002/adem.201700645.
[26] C. Suryanarayana, Mechanical alloying and milling, Prog. Mater. Sci. 46 (2001) 1–184. https://doi.org/10.1016/S0079-6425(99)00010-9.
[27] M. Vaidya, G.M. Muralikrishna, B.S. Murty, High-entropy alloys by mechanical alloying: A review, J. Mater. Res. 34 (2019) 664–686. https://doi.org/10.1557/jmr.2019.37.
[28] M.C. Gao, P.K. Liaw, J.W. Yeh, Y. Zhang, High-entropy alloys: Fundamentals and applications, 2016. https://doi.org/10.1007/978-3-319-27013-5.
[29] S. Uporov, V. Bykov, S. Pryanichnikov, A. Shubin, N. Uporova, Effect of synthesis route on structure and properties of AlCoCrFeNi high-entropy alloy, Intermetallics. 83 (2017) 1–8. https://doi.org/10.1016/j.intermet.2016.12.003.
[30] S. Syed Ghazi, K.R. Ravi, Phase-evolution in high entropy alloys: Role of synthesis route, Intermetallics. 73 (2016) 40–42. https://doi.org/10.1016/j.intermet.2016.03.002.
[31] C. Suryanarayana, F.H. Froes, Mechanical Alloying of Titanium-Base Alloys, Adv. Mater. 5 (1993) 96–106. https://doi.org/10.1002/adma.19930050205.
[32] R. John, A. Karati, M.M. Garlapati, M. Vaidya, R. Bhattacharya, D. Fabijanic, B.S. Murty, influence of mechanically activated annealing on phase evolution in Al0.3CoCrFeNi high-entropy alloy, J. Mater. Sci. 54 (2019) 14588–14598. https://doi.org/10.1007/s10853-019-03917-7.
[33] Y. Xie, H. Cheng, Q. Tang, W. Chen, W. Chen, P. Dai, Effects of N addition on microstructure and mechanical properties of CoCrFeNiMn high entropy alloy produced by mechanical alloying and vacuum hot pressing sintering, Intermetallics. 93 (2018) 228–234. https://doi.org/10.1016/j.intermet.2017.09.013.

[34] B. Kang, J. Lee, H.J. Ryu, S.H. Hong, Ultra-high strength WNbMoTaV high-entropy alloys with fine grain structure fabricated by powder metallurgical process, Mater. Sci. Eng. A. 712 (2018) 616–624. https://doi.org/10.1016/j.msea.2017.12.021.
[35] J. Pan, T. Dai, T. Lu, X. Ni, J. Dai, M. Li, Microstructure and mechanical properties of Nb25Mo25Ta25W25 and Ti8Nb23Mo23Ta23W23 high entropy alloys prepared by mechanical alloying and spark plasma sintering, Mater. Sci. Eng. A. 738 (2018) 362–366. https://doi.org/10.1016/j.msea.2018.09.089.
[36] S.W. Xin, M. Zhang, T.T. Yang, Y.Y. Zhao, B.R. Sun, T.D. Shen, Ultrahard bulk nanocrystalline VNbMoTaW high-entropy alloy, J. Alloys Compd. 769 (2018) 597–604. https://doi.org/10.1016/j.jallcom.2018.07.331.
[37] G. Wang, Q. Liu, J. Yang, X. Li, X. Sui, Y. Gu, Y. Liu, Synthesis and thermal stability of a nanocrystalline MoNbTaTiV refractory high-entropy alloy via mechanical alloying, Int. J. Refract. Met. Hard Mater. 84 (2019) 104988. https://doi.org/10.1016/j.ijrmhm.2019.104988.
[38] J.A. Smeltzer, C.J. Marvel, B.C. Hornbuckle, A.J. Roberts, J.M. Marsico, A.K. Giri, K.A. Darling, J.M. Rickman, H.M. Chan, M.P. Harmer, Achieving ultra hard refractory multi-principal element alloys via mechanical alloying, Mater. Sci. Eng. A. 763 (2019). https://doi.org/10.1016/j.msea.2019.138140.
[39] V. Soni, B. Gwalani, O.N. Senkov, B. Viswanathan, T. Alam, D.B. Miracle, R. Banerjee, Phase stability as a function of temperature in a refractory high-entropy alloy, J. Mater. Res. 33 (2018) 3235–3246. https://doi.org/10.1557/jmr.2018.223.
[40] S. Praveen, A. Anupam, R. Tilak, R.S. Kottada, Phase evolution and thermal stability of AlCoCrFe high entropy alloy with carbon as unsolicited addition from milling media, Mater. Chem. Phys. 210 (2018) 57–61. https://doi.org/10.1016/j.matchemphys.2017.10.040.
[41] P. Sathiyamoorthi, J. Basu, S. Kashyap, K.G. Pradeep, R.S. Kottada, Thermal stability and grain boundary strengthening in ultrafine-grained CoCrFeNi high entropy alloy composite, Mater. Des. 134 (2017) 426–433. https://doi.org/10.1016/j.matdes.2017.08.053.
[42] S. Praveen, J. Basu, S. Kashyap, R. Sankar, Exceptional resistance to grain growth in nanocrystalline CoCrFeNi high entropy alloy at high homologous temperatures, J. Alloys Compd. 662 (2016) 361–367. https://doi.org/10.1016/j.jallcom.2015.12.020.
[43] S. Lv, Y. Zu, G. Chen, X. Fu, W. Zhou, An ultra-high strength CrMoNbWTi-C high entropy alloy co-strengthened by dispersed refractory IM and UHTC phases, J. Alloys Compd. 788 (2019) 1256–1264. https://doi.org/10.1016/j.jallcom.2019.02.318.
[44] L. Raman, K. Guruvidyathri, G. Kumari, S.V.S. Narayana Murty, R.S. Kottada, B.S. Murty, Phase evolution of refractory high-entropy alloy CrMoNbTiW during mechanical alloying and spark plasma sintering, J. Mater. Res. 34 (2019) 756–766. https://doi.org/10.1557/jmr.2018.483.
[45] H. Conrad, Effect of interstitial solutes on the strength and ductility of titanium, Prog. Mater. Sci. 26 (1981) 123–403. https://doi.org/10.1016/0079-6425(81)90001-3.
[46] W. Sun, X. Huang, A.A. Luo, Phase formations in low density high entropy alloys, CALPHAD Comput. Coupling Phase Diagrams Thermochem. 56 (2017) 19–28. https://doi.org/10.1016/j.CALPHAD.2016.11.002.
[47] R. Raghavan, K.C. Hari Kumar, B.S. Murty, Analysis of phase formation in multi-component alloys, J. Alloys Compd. 544 (2012) 152–158. https://doi.org/10.1016/j.jallcom.2012.07.105.
[48] N. Saunders and A. P. Miodownik, CALPHAD (calculation of phase diagrams): A comprehensive guide, Elsevier, 1998.
[49] B. Sundman, B. Jansson, and J. O. Andersson, The Thermo-Calc databank system.,

CALPHAD. 9 (1985) 153–190.
[50] K. Guruvidyathri, B.S. Murty, J.W. Yeh, K.C. Hari Kumar, Gibbs energy-composition plots as a tool for high-entropy alloy design, J. Alloys Compd. 768 (2018) 358–367. https://doi.org/10.1016/j.jallcom.2018.07.264.
[51] C. Vahlas, B. Drouin Ladouce, P.-Y. Chevalier, C. Bernard, L. Vandenbulcke, A thermodynamic evaluation of the Ti-N system, Thermochim. Acta. 180 (1991) 23–37. https://doi.org/10.1016/0040-6031(91)80371-O.
[52] D.R. Gaskell, Introduction to the Thermodynamics of Solids, Fourth, Taylor & Francis, Great Britain, 2009. https://doi.org/10.1115/1.2901487.
[53] S.G. Seo, C.H. Park, H.Y. Kim, W.H. Nam, M. Jeong, Y.N. Choi, Y.S. Lim, W.S. Seo, S.J. Kim, J.Y. Lee, Y.S. Cho, Preparation and visible-light photocatalysis of hollow rock-salt TiO 1-xNx nanoparticles, J. Mater. Chem. A. 1 (2013) 3639–3644. https://doi.org/10.1039/c3ta00936j.
[54] H.O. Pierson, Handbook of refractory carbides and nitrides : properties, characteristics, processing, and applications, Handb. Refract. Carbides Nitrides. (1996) 362. https://doi.org/10.1016/B978-081551392-6.50005-2.
[55] LeClaire, A. D., Diffusion of C, N, and O metals, Diffus. Solid Met. Alloy. (1990) 471–472. https://doi.org/10.1007/10390457_89.
[56] W. Guo, S. Martelli, F. Padella, M. Magini, N. Burgio, E. Paradiso, U. Franzoni, F.C.C. Metastable Phase Induced in the Ti-Al System by Mechanical Alloying of Pure Elemental Powders, Mater. Sci. Forum. 88–90 (1992) 139–146. https://doi.org/10.4028/www.scientific.net/msf.88-90.139.
[57] M. Cancarevic, M. Zinkevich, F. Aldinger, Thermodynamic description of the Ti-O system using the associate model for the liquid phase, CALPHAD Comput. Coupling Phase Diagrams Thermochem. 31 (2007) 330–342. https://doi.org/10.1016/j.CALPHAD.2007.01.009.
[58] H. Bhadeshia, R. Honeycombe, Strengthening of Iron and Its Alloys, in: H. Bhadeshia, R.B.T.-S.M. and P. (Fourth E. Honeycombe (Eds.), Steels Microstruct. Prop., Elsevier, 2017: pp. 23–57. https://doi.org/10.1016/B978-0-08-100270-4.00002-0.
[59] J. Liu, C. Chen, Y. Xu, S. Wu, G. Wang, H. Wang, Y. Fang, L. Meng, Deformation twinning behaviors of the low stacking fault energy high-entropy alloy: An in-situ TEM study, Scr. Mater. 137 (2017) 9–12. https://doi.org/10.1016/j.scriptamat.2017.05.001.
[60] D. Hull, D.J. Bacon, Introduction to Dislocations, 5th ed., Elsevier, 2011. https://doi.org/10.1016/C2009-0-64358-0.
[61] K. Momma, F. Izumi, VESTA 3 for three-dimensional visualization of crystal, volumetric and morphology data, J. Appl. Crystallogr. 44 (2011) 1272–1276. https://doi.org/10.1107/S0021889811038970.
[62] D. Hull, D.J. Bacon, Chapter 6 - Dislocations in Other Crystal Structures, in: D. Hull, D.J. Bacon (Eds.), Introd. to Dislocations (Fifth Ed., Fifth Edit, Butterworth-Heinemann, Oxford, 2011: pp. 109–136. https://doi.org/https://doi.org/10.1016/B978-0-08-096672-4.00006-2.
[63] S. Shi, L. Zhu, H. Zhang, Z. Sun, R. Ahuja, Mapping the relationship among composition, stacking fault energy and ductility in Nb alloys: A first-principles study, Acta Mater. 144 (2018) 853–861. https://doi.org/10.1016/j.actamat.2017.11.029.

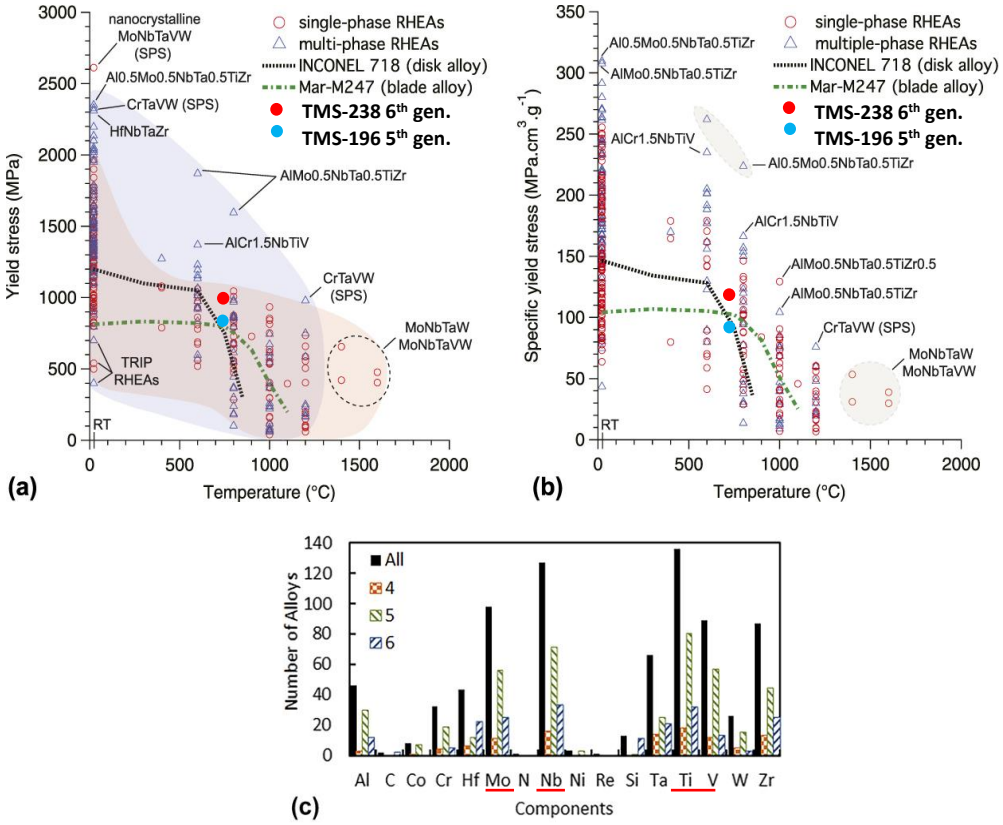

Figure 1: (a) Yield strength and (b) Specific Yield strength as function of temperature. (c) Distribution of alloying elements in RHEAs.

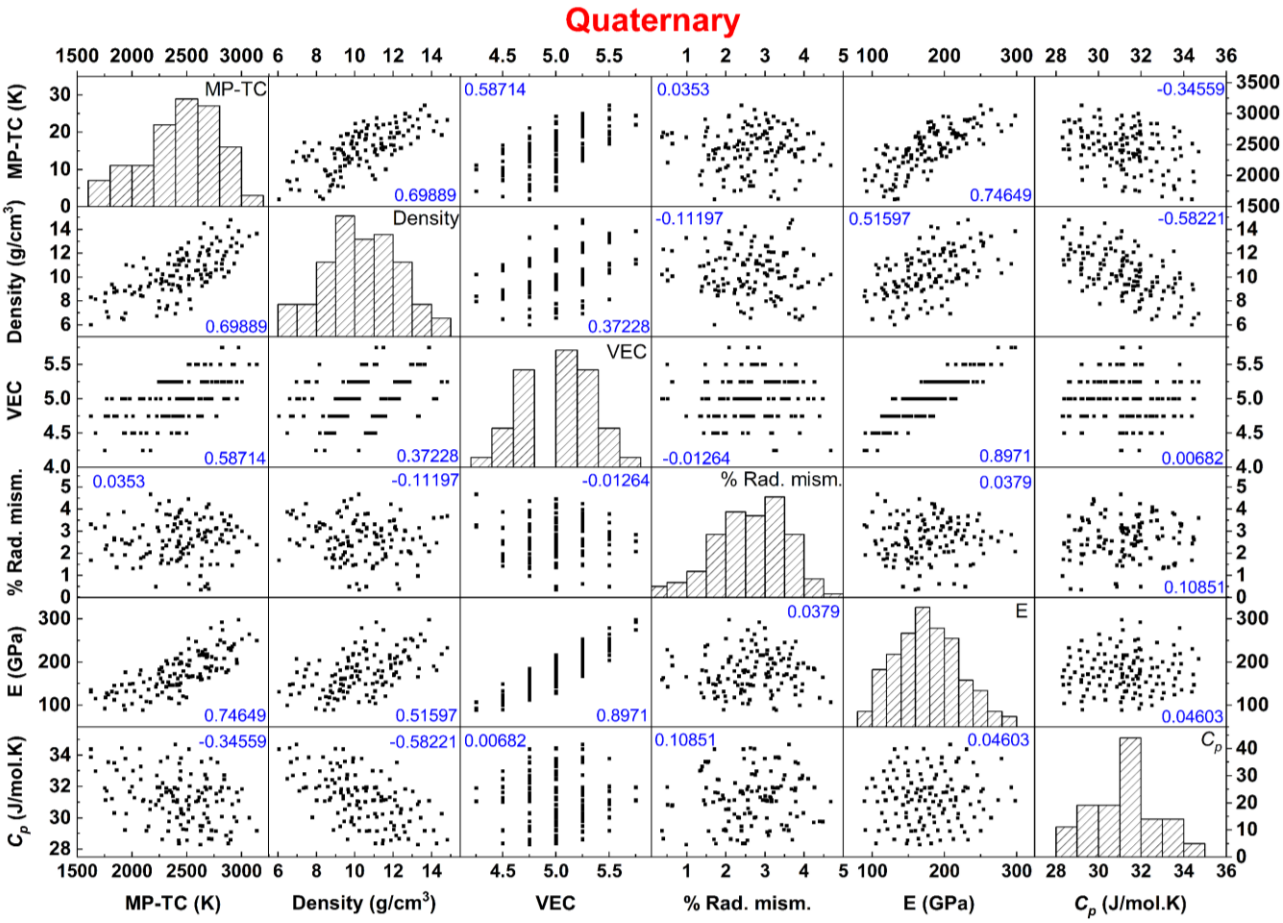

Fig. 2: Scatter matrix plot of 4RHEAs.

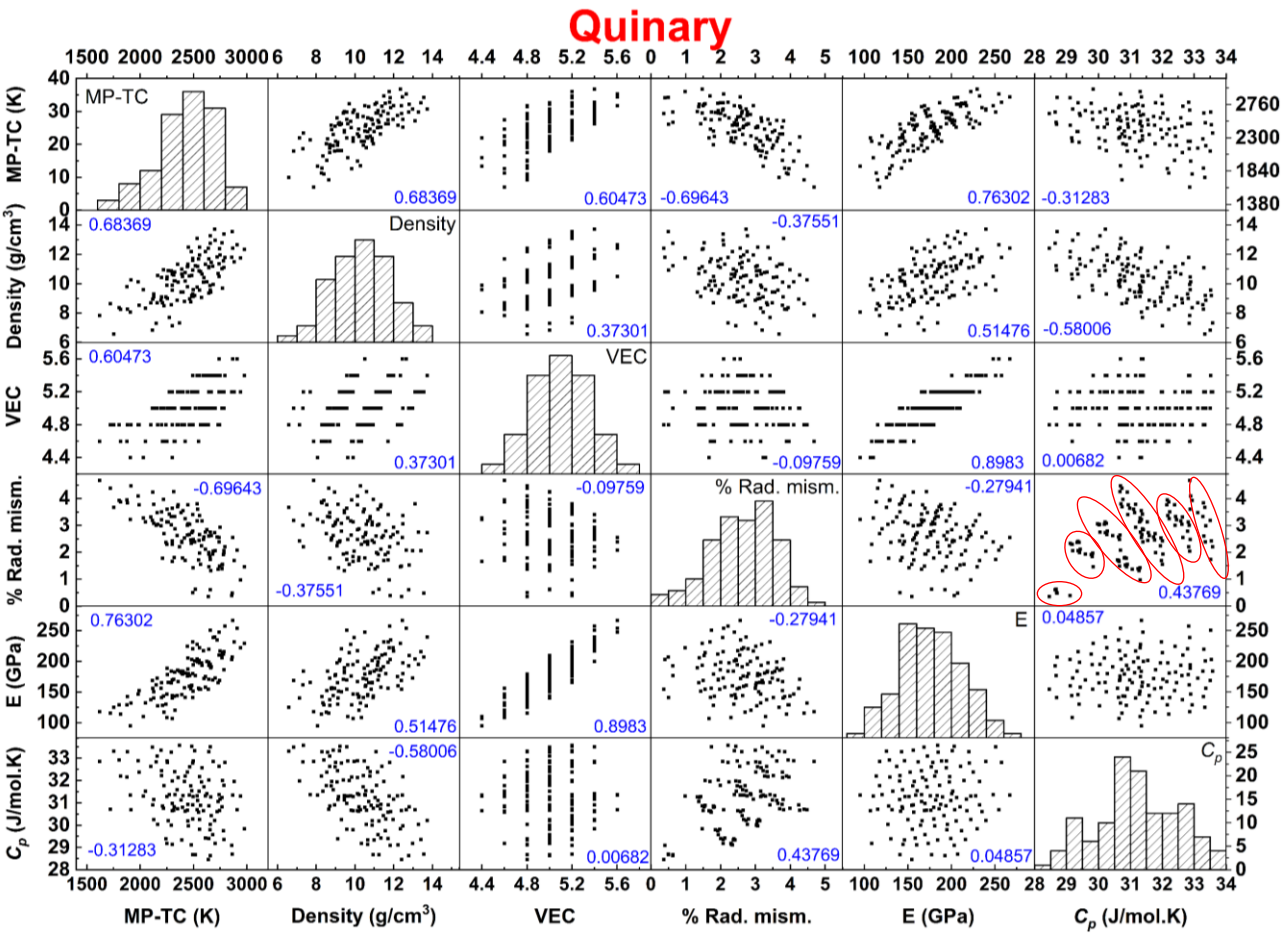

Fig. 3: Scatter matrix plot of 5RHEAs.

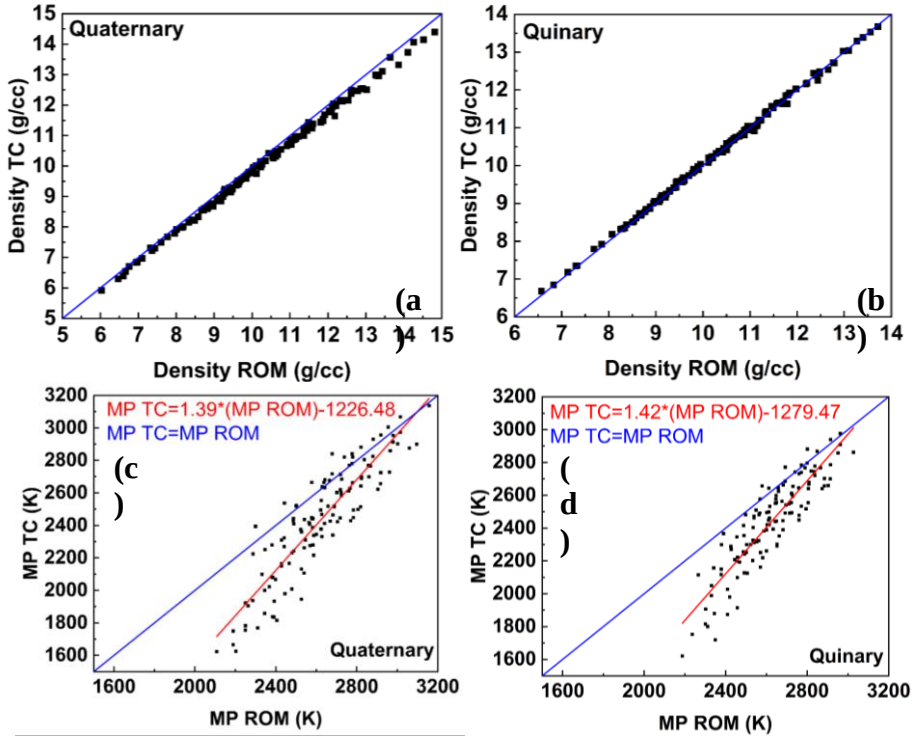

Fig. 4: CALPHAD and ROM calculated density comparison for (a) 4RHEAs (b) 5RHEAs.

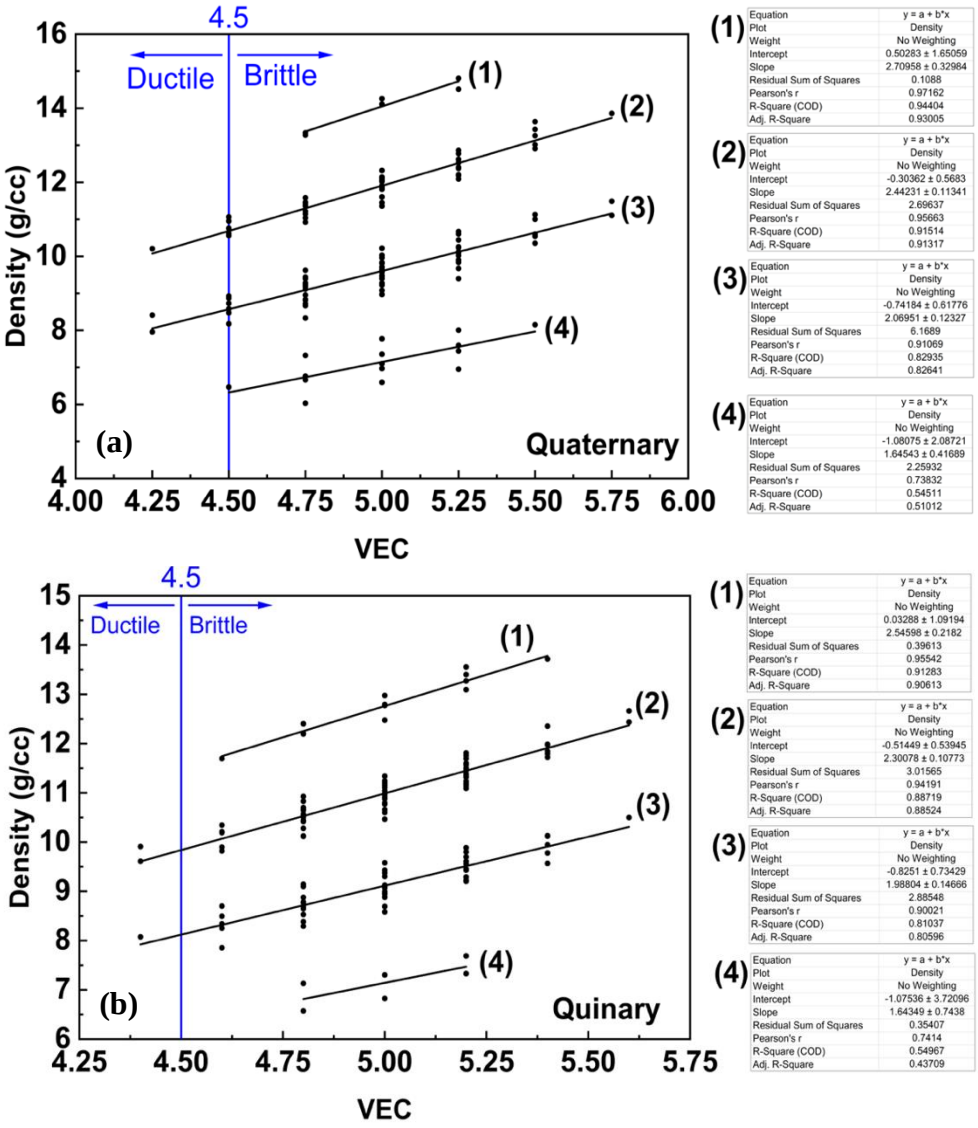

Fig. 5: Density correlated with VEC for (a) 4RHEAs (b) 5RHEAs.

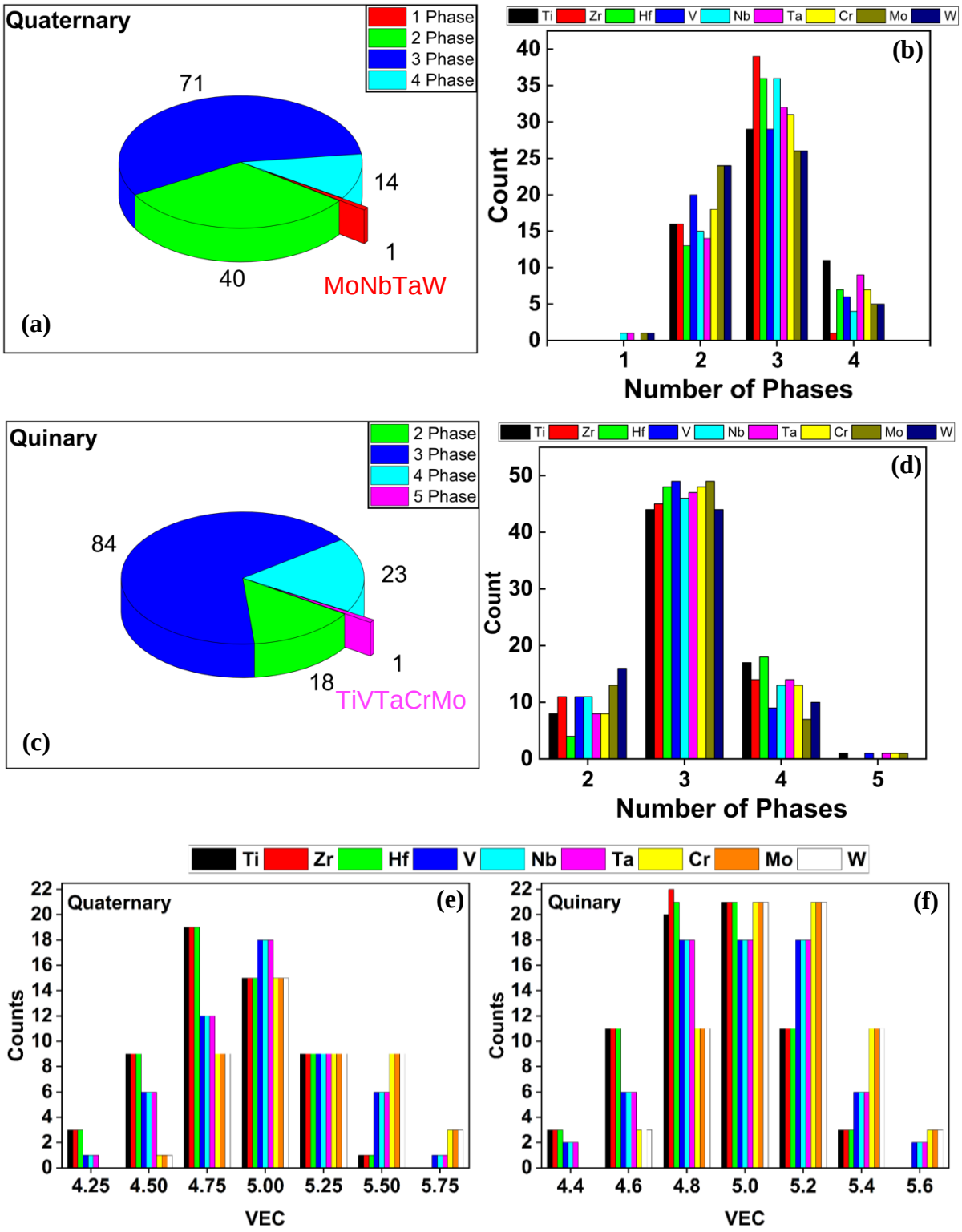

Fig. 6: (a) Count of RHEAs with different number of phases. (b) Element counts in 1/2/3/4 phase 4RHEAs. (c) Count of RHEAs with different number of phases. (d) Element counts in 2/3/4/5 phase 5RHEAs. (e) Element counts in 4RHEAs of different VEC values

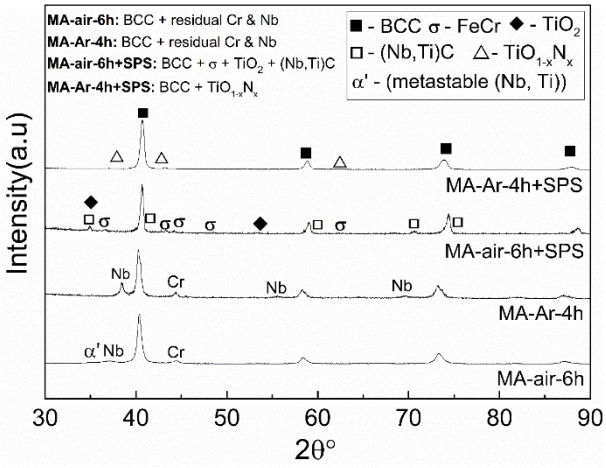

Fig. 7: XRD patterns of the MA powder (MA-air-6h and MA-Ar-4h) and sintered samples (MA-air-6h+SPS and MA-Ar-4h+SPS) showing the formation of secondary phases due to contamination from milling media and atmosphere

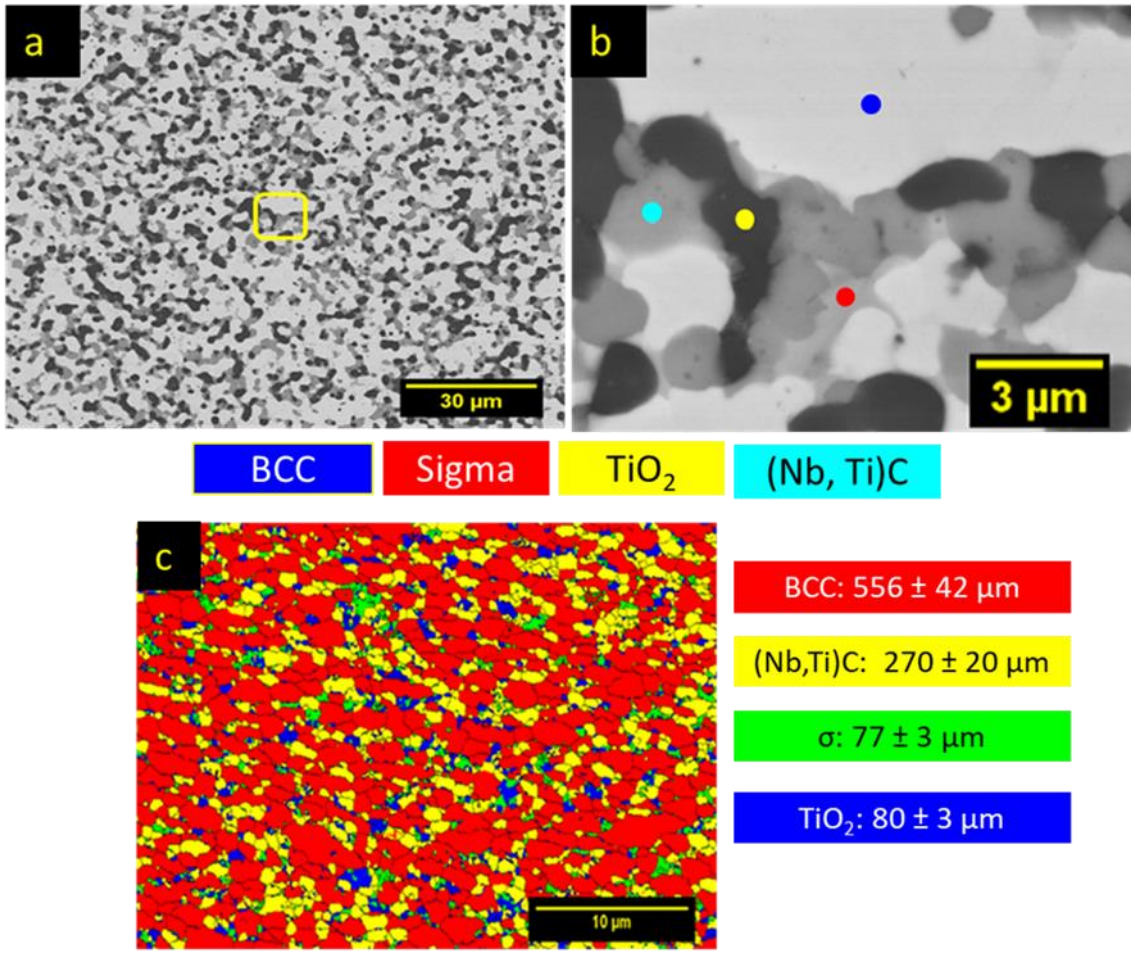

Fig. 8: (a) Lower magnification BSE-SEM micrograph of the MA-air-6h powder after sintering at 1300 °C and 50 MPa, (b) magnified image of the region inside the yellow box. (c) Phase map of the MA-air-6h+SPS CrMoNbTiW obtained via EBSD featuring the BCC, sigma, carbide, and oxide phases in red, green, yellow, and blue color, respectively, along with their grain size.

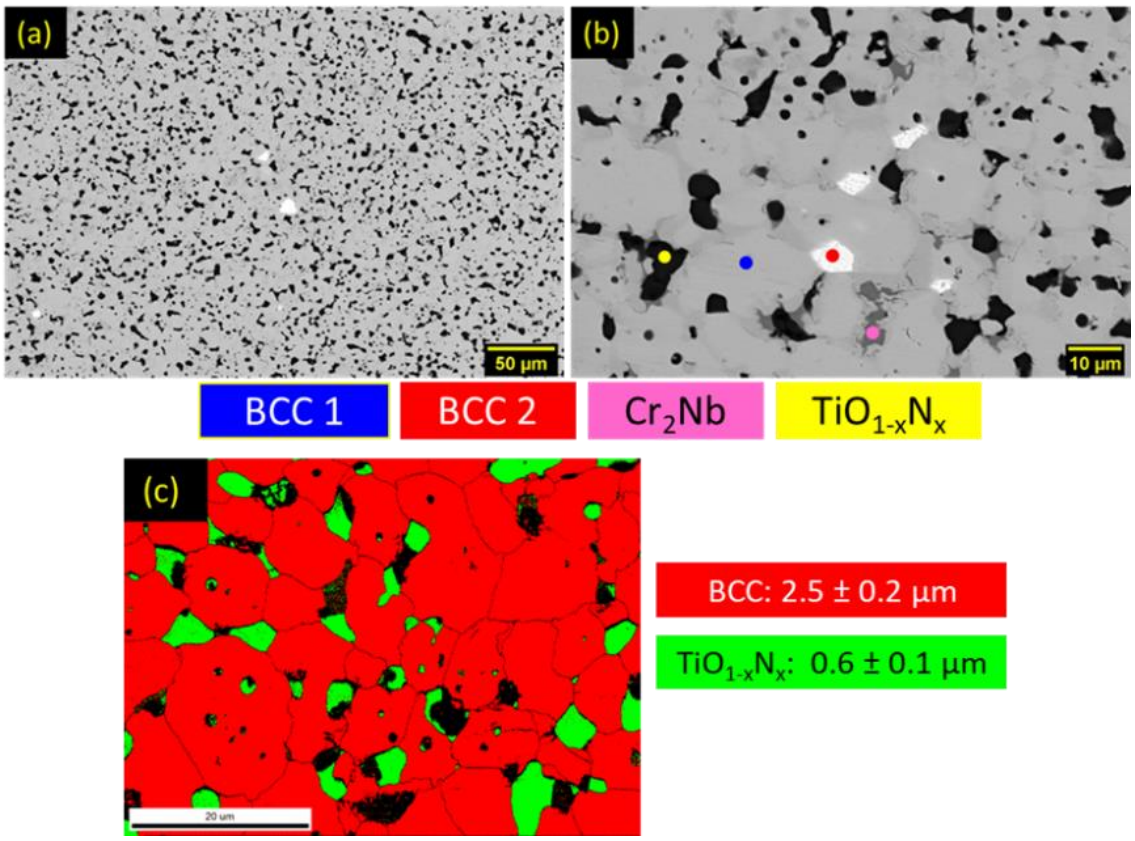

Fig. 9: (a) Lower magnification BSE-SEM micrograph of the MA-Ar-4h powder after sintering at 1500 °C and 50 MPa, (b) magnified image showing different phases. Blue, red, yellow, and pink dots represent grey (BCC1), white (BCC2), black ($TiO_{1-x}N_x$), and dark grey (Laves phase), respectively, and (c) Phase map of the MA-Ar-4h+SPS CrMoNbTiW obtained through EBSD featuring the BCC and $TiO_{1-x}N_x$ phases in red and green color, respectively.

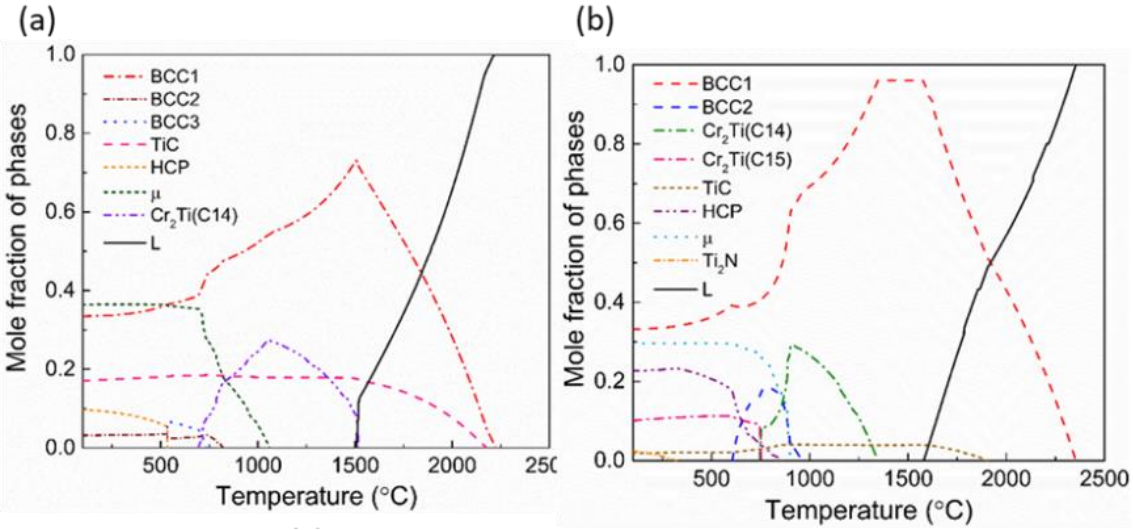

Fig. 6: Calculated phase fraction plot of (a) MA-air-6h+SPS and (b) MA-Ar-4h+SPS with C, and Fe and C, N, and Fe addition, respectively, to account for the formation of secondary phases, using TCHEA (v2.1).

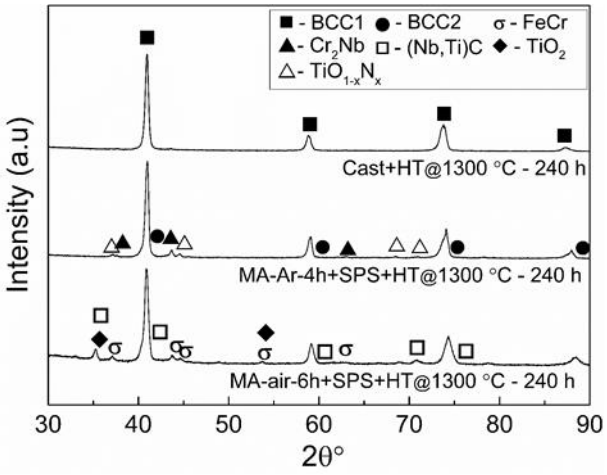

Fig. 7: XRD pattern of CrMoNbTiW alloy synthesized through different routes after heat-treatment at 1300 °C for 240h illustrating the absence of any new phase formation.

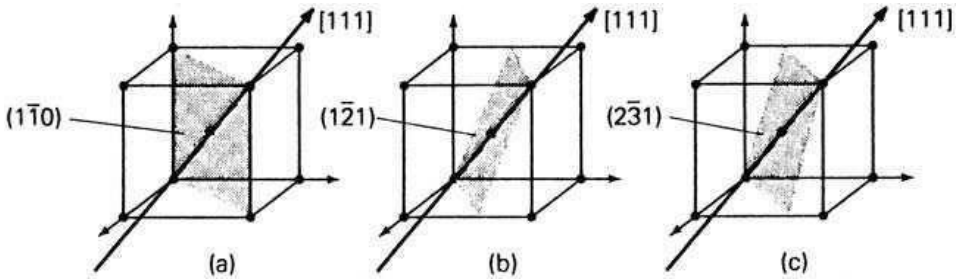

Fig. 8: Slip planes in BCC with common slip direction [111].

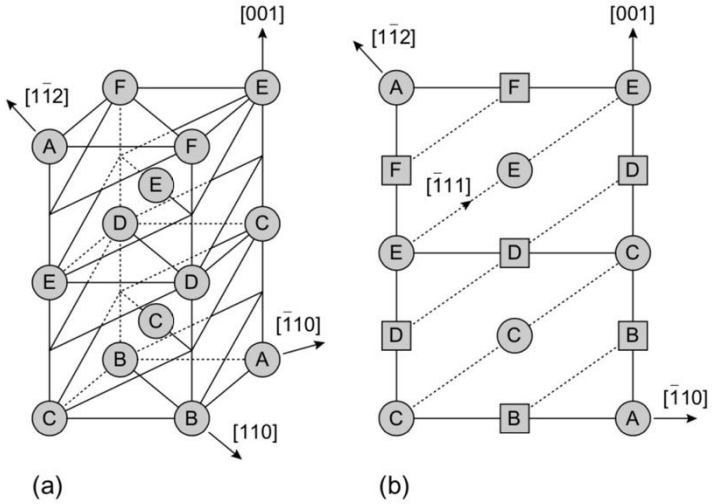

Fig. 9: (112) plane stacking sequence in BCC crystal.

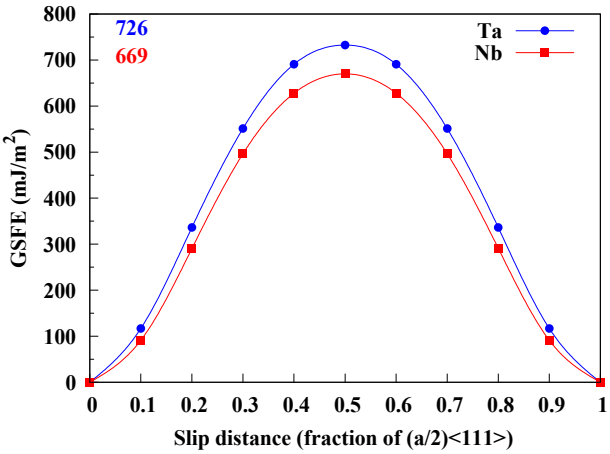

Fig. 10: {110}<111> GSFE curve of Ta and Nb.

LIST OF SYMBOLS, ABBREVIATIONS, AND ACRONYMS

4RHEAs	quaternary RHEAs
5RHEAs	quinary RHEAs
BCC	Body centered cubic
BDT	Brittle to ductile transition
BSE	Back-scattered electron
CALPHAD	Calculation of Phase Diagram
Cp	specific heat at constant pressure
DBTT	ductile to brittle transition temperature
EBSD	electron back-scattered diffraction
EDS	Energy dispersive spectroscopy
FCC	Face centered cubic
FE-SEM	Field emission SEM
FEG	Field emission
GSFE	generalized stacking fault energy
HCP	Hexagonal close packed
HEAs	High Entropy Alloys
ICSD	Inorganic crystal structure database
MA	Mechanical Alloying
MA-Air	MA in Air atmosphere
MA-Ar	MA in Argon atmosphere
MA+SPS	MA followed by SPS
PCA	Process control agent
RHEAs	Refractory HEAs
ROM	Rule-of-mixtures
RT	Room temperature
SEM	Scanning electron microscope
SFE	Stacking fault energy
SPS	Spark Plasma Sintering
SS	Stainless steel
TCHEA	Thermo-Calc High Entropy Alloy database
VAM	Vacuum arc melting
VEC	Valence electron concentration
XRD	X-ray diffraction
E	Young’s modulus
δ	% atomic size difference
ρ	density